Check for
updates

Numerical investigation of wall pressure fluctuations for zero and adverse pressure gradient turbulent boundary layers using synthetic anisotropic turbulence

Nan Hu[*], Nils Reiche[†] and Roland Ewert[‡]

German Aerospace Center (DLR), Technical Acoustics Branch, Braunschweig, Germany

Pressure fluctuations within turbulent boundary layers on a flat plate configuration are simulated using synthetic isotropic and anisotropic turbulence generated by the Fast Random Particle-Mesh Method. The averaged turbulence statistics needed for the stochastic realization is provided by a Reynolds averaged Navier-Stokes calculation. Different integral length scales in different directions are used to realize the anisotropy of the turbulence length scales. Reynolds stress anisotropy is implemented by relating the anisotropic Reynolds stresses obtained from the Reynolds averaged Navier-Stokes calculation and the respective isotropic Reynolds stresses realized from the Fast Random Particle-Mesh Method. Wall pressure fluctuations are obtained by solving a Poisson equation including both the mean-shear turbulence interaction source term and the turbulence-turbulence interaction source term. The Poisson equation is solved using the convolution theorem in wavenumber domain and with a free-space Green function. For an exact realization of the Green function in conjunction with a Fourier transform method on a finite domain, Hockney's method is applied to the Poisson problem. Wall pressure fluctuations for zero and adverse pressure gradient boundary layers are calculated. The adverse pressure gradient is realized by placing an airfoil above the flat plate. Simulated one-point spectra and two-point statistics are analyzed. Simulated results for the wall pressure one-point spectra show that spectra from both the mean-shear term and the turbulence-turbulence term have the same order of magnitude. The results are compared to the experimental results, which were acquired in the Acoustic Windtunnel Braunschweig for the same configurations.

I. Introduction

Wall pressure fluctuations beneath a turbulent boundary layer is one of the major source for vehicle and aircraft cabin noise. Not only the pressure fluctuation magnitude but also the spatial and temporal properties of the fluctuations are relevant for the resulting surface vibration and the noise radiated into the cabin. The two-point correlation in longitudinal and lateral direction and the convective velocity of the surface fluctuating pressure field are the most relevant features for representing the spatial and temporal properties of the pressure field. A comprehensive overview on the subject of wall pressure fluctuations, induced surface vibration and sound radiation was given in the monograph of Blake.[1] Many experiments for measuring the one-point and two-point statistics beneath zero pressure gradient (ZPG) and non-ZPG boundary layers have been carried out.[2–12] Several spectral models for one-point spectra were proposed, e.g. for ZPG by[13–18] and for adverse pressure gradient (APG) by.[12,19–22] The most used model for describing the spatial and temporal properties of the wall fluctuating pressure field is the one proposed by Corcos,[23] which uses exponential functions to represent the coherence decay in both streamwise and lateral directions. Effects of pressure gradient on the spatial and temporal properties are studied by.[4,12,21]

Turbulent boundary layers have been simulated by using direct numerical simulation (DNS) or large eddy simulation (LES) over the past few decades.[24–34] Some features of wall pressure fluctuations can be

---

[*]Research scientist, AIAA member, nan.hu@dlr.de
[†]Research scientist, AIAA member, nils.reiche@dlr.de
[‡]Senior scientist, AIAA Senior member, roland.ewert@dlr.de

studied through numerical work, which are not possible or very difficult to measure in experiments. One example is the investigation of the mean-shear turbulence interaction term and the turbulence-turbulence interaction term. Before turbulent boundary layers could be studied numerically, only few theoretical works[13, 35–37] on this issue were published and it is commonly believed that the mean-shear term is the dominant part for the wall pressure fluctuations. However, recent numerical studies show different results, which show a comparable level between both terms.[25, 28, 38, 39] Although the turbulent boundary layer can be simulated by DNS and LES, due to the extremely expensive computational resources, applications are generally restricted to generic studies at low and medium Reynolds numbers. A more efficient approach for the simulation of turbulent boundary layers was published by Hu *et al.*,[39, 40] which is also applicable for computations at higher Reynolds numbers. Turbulence within the boundary layer is not resolved by this approach, but generated by the Fast Random Particle-Mesh Method (FRPM). The fluctuating pressure within the boundary layer is calculated via a Poisson equation using synthetic turbulence. Both the mean-shear and the turbulence-turbulence terms were considered. The equation was solved by using a free-space Green function and solving the convolution with a spatial fast Fourier transform utilizing Hockney's method.[41]

In the present work, ZPG boundary layers with two different velocities and an APG boundary layer are computed using the same numerical procedure as in Hu *et al.*.[39] Results from the synthetic anisotropic turbulence approach for one-point spectra, cross spectra and convective velocities of the wall pressure fluctuations are analyzed and compared to the experimental results from Hu and Herr.[12] In addition, a comparison between both anisotropic and isotropic turbulence approaches is made. Properties of the mean-shear term and the turbulence-turbulence term are discussed. The method is briefly described in section II. The numerical setups and the flow conditions for the calculated cases are presented in section III. The results are discussed and compared to the experimental results in section IV.

II.   Numerical approach

A.   Poisson equation

Pressure fluctuations in an incompressible turbulent boundary layer are governed by a Poisson equation. For a turbulent boundary layer along a wall located at $x_2 = 0$, refer to Fig. 1, the Poisson equation resulting from a mean-flow in positive x_1-direction, becomes

$$\Delta p = -\rho_0 \left(2 \frac{\partial U_1}{\partial x_2} \frac{\partial u_2}{\partial x_1} + \frac{\partial^2}{\partial x_i \partial x_j} (u_i u_j - \overline{u_i u_j}) \right). \tag{1}$$

Here, U_1 denotes the mean-flow velocity component in x_1-direction and u_i indicates velocity fluctuations; ρ_0 is the mean air density and p is the fluctuating pressure. The source term on the right-hand side of Eq. (1) comprises two parts. The first part is the mean-shear turbulence interaction term and the second part is the turbulence-turbulence interaction term. If the boundary is a rigid flat surface, the fluctuating pressure can be calculated using an integral of the free-space Green function with the right-hand side source terms, i.e.,

$$p(\mathbf{x}, t) = -\int_{\mathbf{V_s} + \mathbf{V_s'}} \rho_0 \left(2 \frac{\partial U_1}{\partial x_2} \frac{\partial u_2(\mathbf{y}, t)}{\partial x_1} + \frac{\partial^2}{\partial x_i \partial x_j} (u_i u_j - \overline{u_i u_j})(\mathbf{y}, t) \right) \cdot g(\mathbf{x} - \mathbf{y}) \, d^3 \mathbf{y}. \tag{2}$$

In Eq. (2) the integration is carried out over the original source area $\mathbf{V_s}$ plus a source area $\mathbf{V_s'}$ that represents an image of $\mathbf{V_s}$ mirrored at the solid wall in order to realize the appropriate wall boundary condition $(\partial p / \partial n)_{x_2=0} = 0$ of the pressure fluctuations.[1] Note that, Eq. (2) is a convolution between the source terms and the free-space Green function. So the equation can be more efficiently solved in wavenumber domain by using the convolution theorem. For an accurate numerical solution with this approach, a good approximation to the free-space Green function is required despite the artificial truncation and periodicity of the Green function represented on a finite computational domain. To circumvent this problem, a modification as introduced by Hockney and Eastwood[41] is applied, which provides an exact realization of the free-space Green function in conjunction with a Fourier transform method on the finite domain. A detailed description of this approach applied to the Poisson problem can be found in Hu *et al.*.[39]

B.   FRPM

To calculate the fluctuating pressure, an appropriate fluctuating velocity field within the turbulent boundary layer is needed. We use the Fast Random Particle-Mesh Method (FRPM)[42] to generate synthetic

turbulent velocity fluctuations to prescribe the right-hand side source term of Eq. (1). FRPM uses averaged turbulence statistics to synthesize the turbulent velocity fluctuations. One and two-point statistics are realized. The basic idea is to generate a fluctuating vector potential ψ_i with three components from a convolution of spatial white noise $\mathcal{U}_i$ with a spatial Gaussian filter kernel G,

$$\psi_i(\mathbf{x},t) = \int_{\mathbf{V_s}} \hat{A}(\mathbf{x})G(\mathbf{x}-\mathbf{x}')\mathcal{U}_i(\mathbf{x}',t)\,d^3\mathbf{x}', \tag{3}$$

with

$$G(\mathbf{x}-\mathbf{x}') = \exp\left(-\frac{\pi}{2}\frac{|\mathbf{x}-\mathbf{x}'|}{l_s^2}\right), \tag{4}$$

where $\hat{A}$ denotes an amplitude function whose appropriate scaling yields the desired variance of ψ_i, $\mathbf{x}$ defines field coordinates of the vector potential and $\mathbf{x}'$ defines white noise field coordinates. Furthermore, l_s is an integral turbulent length scale determined from the Reynolds averaged Navier-Stokes (RANS) calculation,

$$l_s^* = \frac{c_l}{C_\mu}\frac{\sqrt{k_t^*}}{\omega^*}, \tag{5}$$

where $k_t^* = k_t/U_{ref}^2$ is the turbulent kinetic energy and $\omega^* = \omega \cdot l_{ref}/U_{ref}$ is the specific rate of dissipation. The expression $*$ denotes non-dimensional parameters. The reference quantities l_{ref} and U_{ref} are set to 1 m and to the sound speed respectively. The constant $C_\mu = 0.09$ and c_l is estimated to be 0.54,[43] so the pre-factor $c_l/C_\mu \simeq 6.0$. An anisotropy of the length scale can be realized by applying a stretching factor γ. It is assumed that the relationship $l_s = (l_1 l_2 l_3)^{1/3}$ and $l_1/\gamma = l_2 = l_3$. Note, the amplitude function $\hat{A}$ is length scale dependant for three dimensional turbulent flows.[42] An individual $\hat{A}_i$ for each direction is needed due to application of the stretching factor. In the present calculation, γ is chosen to be 1.5 which is based on the best practice results according to Hu et $al.$.[39] Note, for an APG boundary layer the value of γ may decrease. However, due to the not very strong APG in the present calculation, the same value of $\gamma = 1.5$ for the APG is used as for the ZPG.

The fluctuating velocities can be obtained by taking the curl of the fluctuating potential field $\boldsymbol{\psi}$,

$$u_i = \epsilon_{ijk}\frac{\partial \psi_k}{\partial x_j}. \tag{6}$$

For sufficiently slow spatially changing length scale l_s and amplitude $\hat{A}$ the derivatives of ψ_i can be expressed through analytical derivatives of the Gaussian filter kernel,

$$u_i(\mathbf{x},t) = \int_{\mathbf{V_s}} \hat{A}(\mathbf{x})\epsilon_{ijk}\frac{\partial G(\mathbf{x}-\mathbf{x}')}{\partial x_j}\mathcal{U}_k(\mathbf{x}',t)\,d^3\mathbf{x}'. \tag{7}$$

The white noise field $\mathcal{U}_i$ is defined in a Lagrangian frame moving at local flow velocity $\mathbf{U}$. Additional temporal turbulence decay can be modeled by a Langevin equation, which introduces the decorrelation in the two-points statistics.[42] Altogether, the cross-correlation properties of the white noise is given by

$$< \mathcal{U}_i(\mathbf{x}',t)\mathcal{U}_j(\mathbf{x}'+\mathbf{r},t+\tau) > = \delta(\mathbf{r}-\mathbf{U}\tau)\exp\left(-\frac{|\tau|}{\tau_s}\right)\delta_{ij}, \tag{8}$$

where the bracket means an ensemble average, δ_{ij} is the Kronecker symbol, $\delta(\mathbf{r}-\mathbf{U}\tau)$ describes a frozen turbulence flow moving with the flow velocity $\mathbf{U}$ and $\exp(-|\tau|/\tau_s)$ involves the turbulence decay, i.e. the spatially white noise is correlated in time with time-scale τ_s. The local time scale can be derived from RANS calculations,

$$\tau_s^* = C_\tau\frac{l_s^*}{\sqrt{k_t^*}}. \tag{9}$$

where the pre-factor C_τ needs to be determined. Tam & Auriault[44] modeled the time-scale in a $k-\epsilon$ model and determined the pre-factor empirically by fitting experimental results of jet flows, which resulted in $C_\tau \simeq 0.91$. Herein, $C_\tau = 1.2$ is applied which was used and obtained by best practices in Hu et $al.$[39] .

Anisotropy of the Reynolds stress is obtained by using a scaling tensor applied to the realized fluctuating velocities from Eq. (7). The scaling tensor can be derived from the relationship between the anisotropic Reynolds stress obtained from the RANS calculations and the respective isotropic expression for the Reynolds stress.

For more details about the FRPM implementation in the computational domain and properties of the generated synthetic turbulence refer to the work of,[42,45] and for the approach of turbulence anisotropy refer to Hu et $al.$.[39]

III.   Computational setups and mean flow conditions

Mean flow statistics are obtained from RANS calculations using DLR's CFD code TAU. The Reynolds stress model with g-equation is used for the computation.[46] The boundary layer is solved on a structured grid with the first cell layer $y^+ < 1$. In total, about 100K grid points are used for the ZPG case and 130K for the APG case, where a grid with 200 nodes is distributed along airfoil upper and lower side respectively. Fig. 1 shows a sketch of the computational domain. The length of the whole plate is 1370 mm with a leading edge length of 120 mm. A 12° beveled trailing edge on the underside of the plate is used to develop a ZPG boundary layer on the topside in the rear area.[47] For the APG case, a NACA-0012 airfoil with a chord length of 400 mm is placed above the flat plate. The rotation axis is at 41% of the chord length. The geometries for the flat plate and the NACA airfoil are identical to those from the experiment from Hu and Herr.[12]
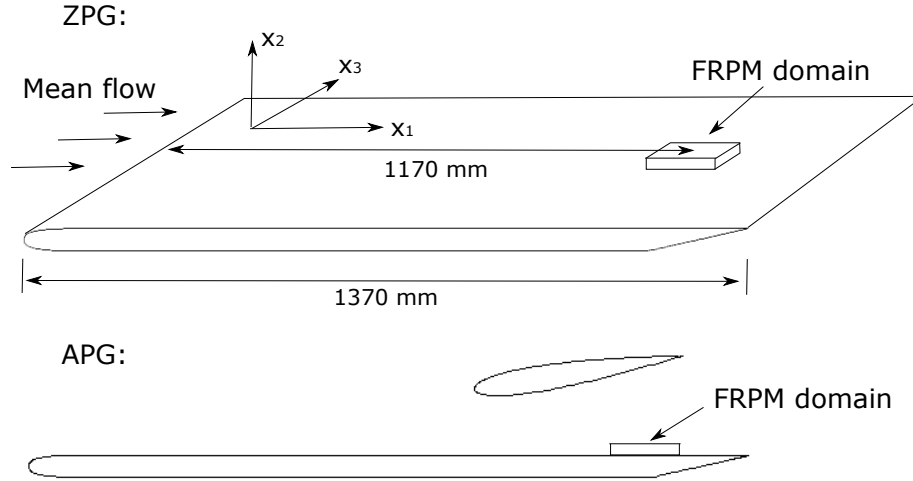

Figure 1: Sketch of the computational domain for the ZPG flow (top) and the side view for the APG case (bottom).

The wall fluctuating pressure beneath the boundary layer is calculated in a three-dimensional rectangular FRPM domain with its center located at $x_1 = 1170$ mm, see Fig. 1. The dimensions of the FRPM domain is $L_1 = 127$ mm, $L_2 = 21$ mm and $L_3 = 63$ mm. Since the Hockney method demands a grid with 2^N mesh points in each direction, a cartesian grid with $128 \times 64 \times 64$ points is used in the calculation. The corresponding mesh size is $\Delta x_1 = \Delta x_3 = 1$ mm and $\Delta x_2 = 1/3$ mm. The calculated boundary layers have similar boundary layer thicknesses, thus, a same sized FRPM domain is used for all the calculation cases. Calculations were carried on a desktop computer equipped with Intel Xeon E5-2630V3 processors. For each case, 4 CPUs (8 threads) was used and about 13000 steps can be calculated per day. The time steps were chosen based on a 'CFL'-like constraint of FRPM,[42] i.e. $\Delta t = 3.21 \times 10^{-5}$ for the case of ZPG for 30.1 m/s, $\Delta t = 1.66 \times 10^{-5}$ for the case of ZPG for 58.8 m/s and $\Delta t = 2.92 \times 10^{-5}$ for the case of APG. In the present work, a one-second simulation was made for each case. The computation time is about 2.5 days for the case with the largest time step and less than 5 days for the case with the finest time step.

The mean velocity profiles were measured at $x_1 = 1210$ mm for ZPG and APG boundary layers and an additional point at $x_1 = 1128$ mm for the APG boundary layer from Hu and Herr.[12] The normalized mean flow velocity profiles from RANS calculations are compared to the measured profiles, shown in Fig. 2. Results from RANS calculations show good agreement with the measured results. Boundary layer parameters obtained from both RANS calculations and the experiment are listed in table 1. Note that, the boundary layer thickness for the APG boundary layer does not match the experimental results. The calculated boundary layer thickness is much thinner than the measured one. This is mainly because the present RANS calculations do not take the open jet wind tunnel environment into account. The presence of the shear layer in the open jet wind tunnel seems to be important for the APG case calculation due to the additional NACA airfoil, although the measured static pressure in the spanwise direction ($\Delta x_3 = 180$ mm at $x_1 = 1110$ mm) showed an almost two-dimensional flow condition in the mid-span region. For the APG calculation case, modifications of the airfoil position are made in order to obtain a similar boundary layer development between $1128 < x_1 < 1210$ mm. In the calculation

American Institute of Aeronautics and Astronautics

Table 1: Comparison of the boundary layer parameters between the results from RANS calculations and the experiment.

|	U_0 (m/s)	δ (mm)	δ^* (mm)	θ (mm)	H	u_τ (m/s)	$Re_\theta = U_0\theta/\nu$
ZPG for two different velocities, $x_1 = 1210$ mm							
RANS	30.1	20.0	3.34	2.42	1.38	1.16	4737
Experiment	30.2	19.7	3.51	2.49	1.41	1.13	4889
RANS	58.8	17.9	2.90	2.15	1.35	2.15	8230
Experiment	58.7	18.5	3.13	2.28	1.37	2.08	8685
APG, $x_1 = 1128$ mm							
RANS	32.9	15.6	3.32	2.09	1.59	0.83	4464
Experiment	32.0	23.0	5.09	3.12	1.63	0.88	6492
APG, $x_1 = 1210$ mm							
RANS	30.4	19.7	5.05	2.93	1.72	0.64	5772
Experiment	30.4	28.7	7.68	4.39	1.75	0.75	8670

(a)

(b)

(c)
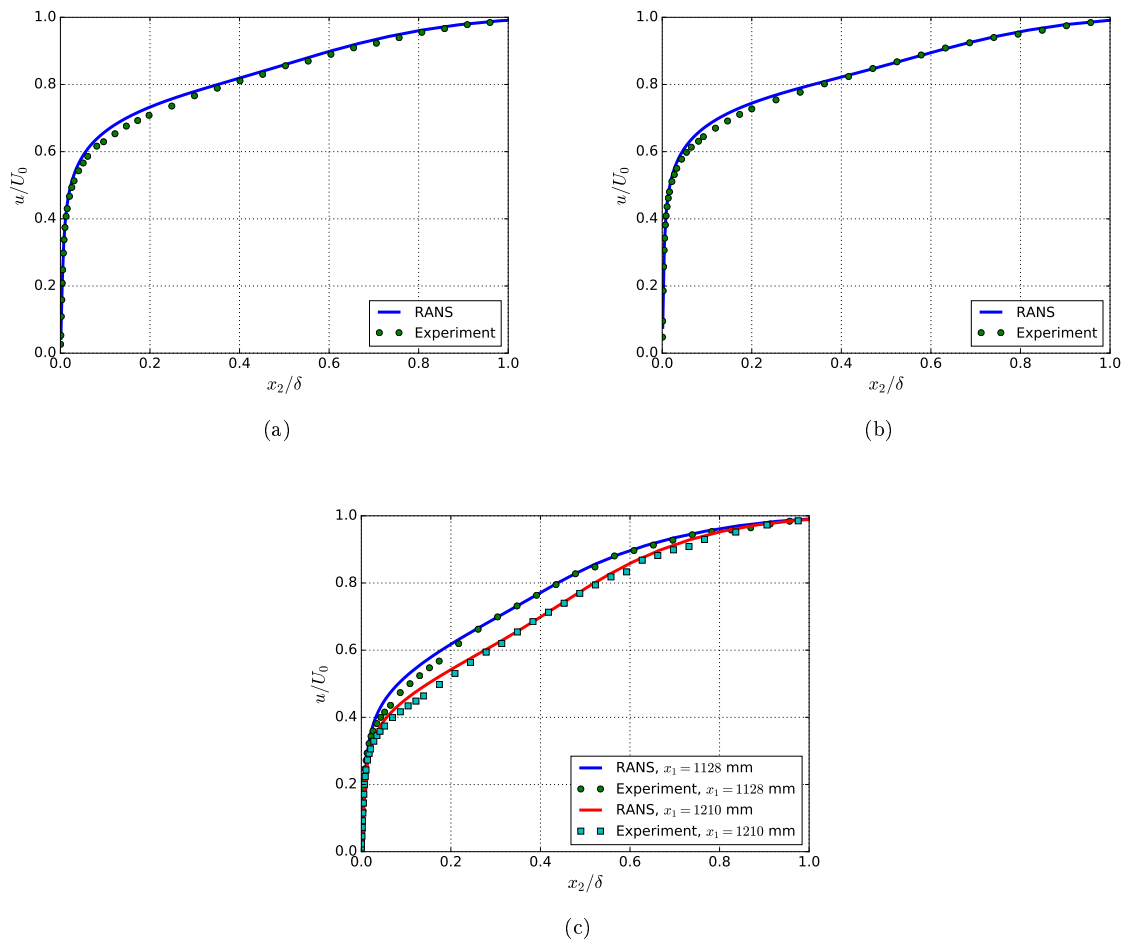
Figure 2: Comparison of the normalized mean velocity profiles between RANS calculations and the experimental results; (a) ZPG for 30.1 m/s at $x_1 = 1210$ mm; (b) ZPG for 58.8 m/s at $x_1 = 1210$ mm; (c) APG at $x_1 = 1128$ mm and 1210 mm.
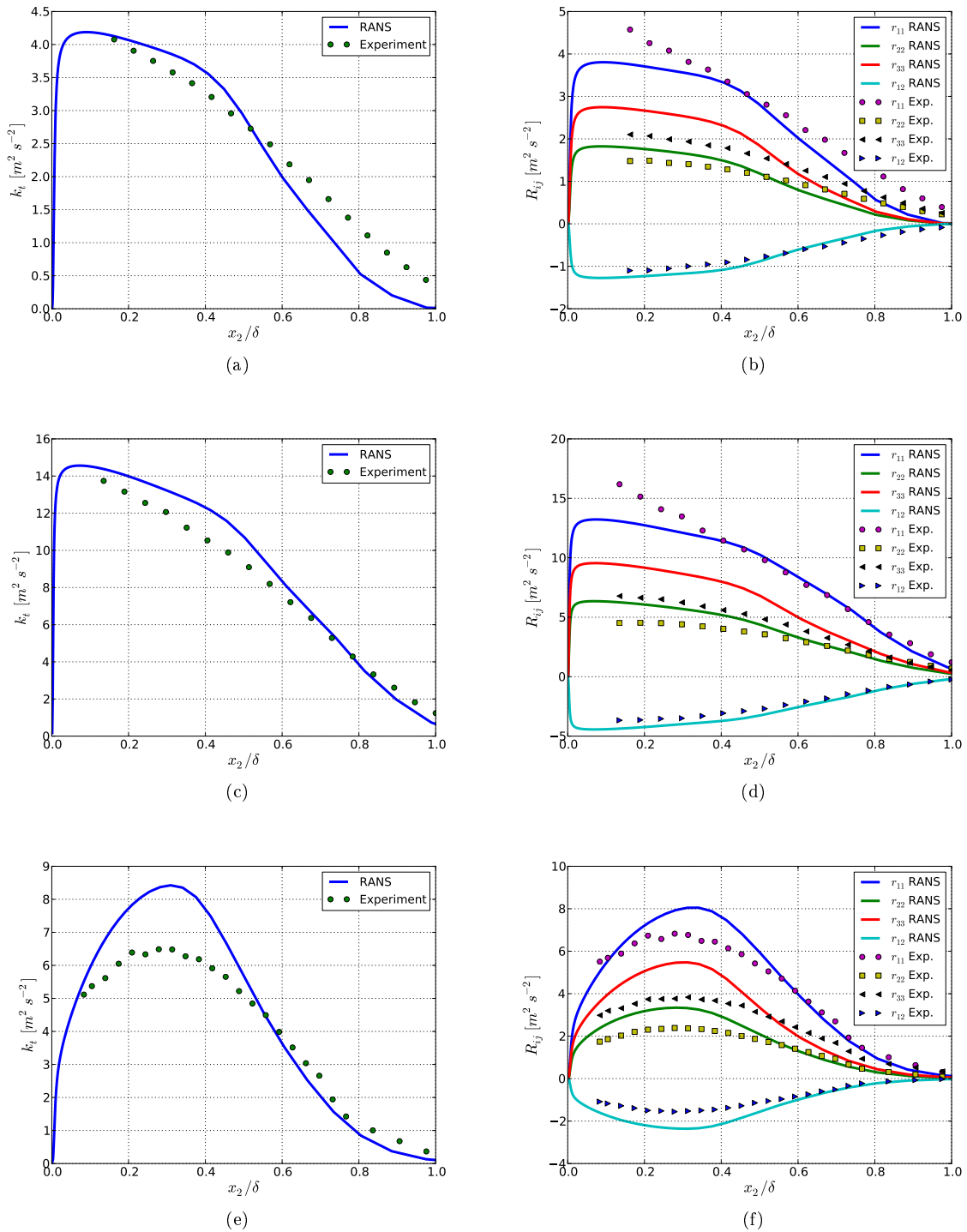
Figure 3: Comparison of the turbulent kinetic energy and the Reynolds stress components between RANS calculations and experimental results at $x_1 = 1210$ mm; (a,b) ZPG for 30.1 m/s; (c,d) ZPG for 58.8 m/s; (e,f) APG.

the rotation axis of the airfoil is located 150 mm above the flat plate while in the measurement 120 mm. The geometric angle of attack of the airfoil is 9° in the calculation while 10° in the measurement.

Comparisons of the turbulent kinetic energy and the Reynolds stress components between RANS calculations and measurement results at $x_1 = 1210$ mm are shown in Fig. 3. For the APG case the kinetic energy was only measured at $x_1 = 1210$ mm in the experiment. In general, the turbulent kinetic energy obtained from RANS calculations show good agreement to the measured data. However, a more rapid decrease trend in the outer region $x_2 > 0.5\delta$ is shown. One reason may be the nearly zero turbulence intensity outside the boundary layer in the calculation domain. This forces the kinetic energy to approach

American Institute of Aeronautics and Astronautics

zero at the boundary layer edge while in the measurement the freestream flow has a larger turbulence intensity. The position of the maximum kinetic energy for the APG boundary layer is well predicted from the RANS calculation, however, the level is larger compared to the measurement. This may be caused by the thinner boundary layer obtained from the RANS calculation. The comparison of the Reynolds stresses shows that for the ZPG cases, r_{22} and r_{33} from the RANS calculations are over-estimated in the near wall region, whereas the r_{11} is under-estimated. A good agreement with the measured results is found for r_{12}. The components $r_{13} = 0$ and $r_{23} = 0$ within a two-dimensional boundary layer.[48] For the APG case all the components are over-estimated due to the reason discussed previously. It should be mentioned that the Reynolds stresses were measured using hot-wire X-probes with an angle of about $6°$ to the flow direction. The measured r_{11} and r_{22} were corrected with the angle correction. However, the value of r_{33} cannot be corrected, which can produce some measurement uncertainties.

IV.   Results

A.   Reynolds stress realization

Turbulence velocity fluctuations realized by FRPM are used to prescribe the fluctuating source terms of the Poisson equation (1). To verify a proper realization of the fluctuating velocity from FRPM, Fig. 4 shows the reconstructed turbulent kinetic energy and Reynolds stress components in comparison to the results from RANS calculations within the boundary layer. A very good reconstruction of the turbulent kinetic energy for the outer region $> 0.3\delta$ is shown in Fig. 4(a) for both the isotropic turbulence approach and the anisotropic turbulence approach (anisotropy of the Reynolds stress and the turbulence length scales). In the inner region, a lack of kinetic energy level is visible. Especially for $< 0.1\delta$, the kinetic energy reconstruction drops dramatically, which is not the case for the RANS calculation. Reason for that could be the used grid resolution is not fine enough to realize the small turbulence structures.

The magnitude of the normal Reynolds stress components r_{ii} are nearly equal realized through the isotropic turbulence approach, see Fig. 4(a). In contrast, using the anisotropic turbulent approach the Reynolds stress components including r_{12} are well reconstructed compared to the RANS calculations, see Fig. 4(b-d).

B.   One-point spectra

The source term of the Poisson equation (1) comprises two contributions, the mean-shear turbulence interaction term and the turbulence-turbulence interaction term. Since the Poisson equation is linear, the pressure fluctuations from both source terms can be separately solved,

$$p_{ms}(\mathbf{x}, t) = -2\rho_0 \int_{\mathbf{V_s}+\mathbf{V_s'}} \frac{\partial U_1}{\partial x_2} \frac{\partial u_2(\mathbf{y}, t)}{\partial x_1} \cdot g(\mathbf{x} - \mathbf{y}) \, d^3\mathbf{y}, \tag{10}$$

$$p_{tt}(\mathbf{x}, t) = -\rho_0 \int_{\mathbf{V_s}+\mathbf{V_s'}} \frac{\partial^2}{\partial x_i x_j} (u_i u_j - \overline{u_i u_j})(\mathbf{y}, t) \cdot g(\mathbf{x} - \mathbf{y}) \, d^3\mathbf{y}, \tag{11}$$

where p_{ms} denotes the pressure fluctuations contributed from the mean-shear term and p_{tt} from the turbulence-turbulence term. Integration by parts can be applied for the calculation of both terms, which can avoid the singularity issue involved by the Green function,[39] reads

$$p_{ms}(\mathbf{x}, t) = 2\rho_0 \int_{\mathbf{V_s}+\mathbf{V_s'}} \frac{\partial U_1}{\partial x_2} u_2(\mathbf{y}, t) \cdot \frac{\partial g(\mathbf{x} - \mathbf{y})}{\partial x_1} \, d^3\mathbf{y}, \tag{12}$$

$$p_{tt}(\mathbf{x}, t) = \rho_0 \int_{\mathbf{V_s}+\mathbf{V_s'}} \frac{\partial}{\partial x_i} (u_i u_j - \overline{u_i u_j})(\mathbf{y}, t) \cdot \frac{\partial g(\mathbf{x} - \mathbf{y})}{\partial x_j} \, d^3\mathbf{y}. \tag{13}$$

The total pressure fluctuations p_{total} can be obtained by

$$p_{total}(\mathbf{x}, t) = p_{ms}(\mathbf{x}, t) + p_{tt}(\mathbf{x}, t). \tag{14}$$

Figure 5 shows simulated one-point spectra of p_{total}, p_{ms} and p_{tt} for different cases. The one-point spectra are calculated with a window length of 512 samples for all the cases. The sampling rate is about 31.2 kHz and 60.2 kHz for ZPG with $U_0 = 30.1$ m/s and $U_0 = 58.8$ m/s and 34.2 kHz for the APG case, which results a frequency resolution of approximately 61 Hz and 118 Hz for the ZPG cases and 67 Hz for the APG case. The spectra of p_{ms} show a maximum at medium frequencies and an increasing behavior at low frequencies, which is due to the term $\partial u_2 / \partial x_1$. Note that, for frozen turbulence the slope at low frequencies should be ω^2, however, due to the temporal turbulence decay the
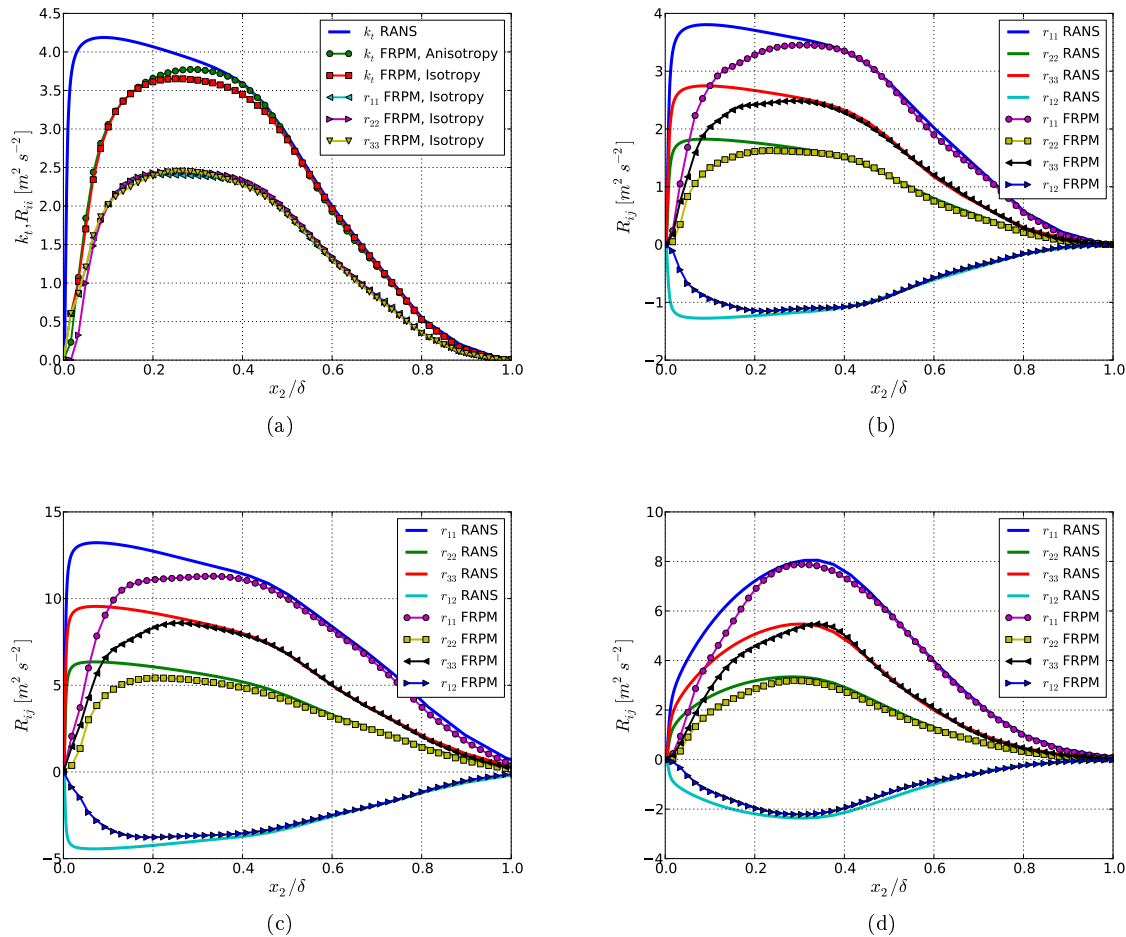
Figure 4: Reconstruction of the turbulent kinetic energy and the Reynolds stress components at $x_1 = 1210$ mm from FPRM in comparison to the results from RANS calculations; anisotropic turbulence approach for (b-d); (a) ZPG for 30.1 m/s; (b) ZPG for 30.1 m/s; (c) ZPG for 58.8 m/s; (d) APG.

slope becomes much flatter for non-frozen turbulence.[13,39,40] In contrast to p_{ms}, spectra of p_{tt} show a rather flat behavior at lower frequencies, which is due to the contribution of terms with no derivative in streamwise direction, i.e. $\partial/\partial x_2 \partial x_2$, $\partial/\partial x_2 \partial x_3$ and $\partial/\partial x_3 \partial x_3$. A comparison between the isotropic and anisotropic turbulence approaches for ZPG case at $U_0 = 30.1$ m/s is given between Figs. 5(a,b). For an isotropic turbulence boundary layer, the results show p_{ms} to be the dominant contribution to the wall pressure fluctuations and the level difference at the spectral peak position between p_{ms} and p_{tt} is about 5 dB. However, when the turbulence anisotropy (both the Reynolds stress and the turbulence length scales) is taken into account, the level difference becomes smaller and is about only 2 dB at the spectral peak position. The results show good agreement with DNS and LES results from numerical works of Kim[25] and Chang *et al.*.[28,38] The spectral level of p_{ms} for anisotropic turbulence decreases, mostly at higher frequencies, compared to isotropic turbulence. In contrast, the level for p_{tt} is almost unchanged, which is probably because the wall pressure fluctuations for p_{tt} is contributed from the entire Reynolds stress components and is insensitive to the ratio of the individual Reynolds stress components. The turbulent kinetic energy is almost equally realized for both isotropic and anisotropic turbulence, and the Reynolds stress component r_{12} present in the anisotropic turbulence is much smaller compared to the kinetic energy, see Fig. 4. The scaled spectra for ZPG cases with different velocities collapse well for all pressure fluctuation parts, i.e. p_{ms}, p_{tt} and p_{total}. The spectral level for the APG case increases and for both p_{ms} and p_{tt} compared to the ZPG case with a comparable velocity, see Figs. 5(b,f). One major reason for the increase of the level is the increase of the velocity fluctuations level. In general, $p_{ms} \sim u_2$ and $p_{tt} \sim u_i u_j$, i.e. p_{tt} increases faster than p_{ms} due to the increase of the velocity fluctuations level. However, the difference of the spectral maximum level between p_{ms} and p_{tt} for the APG case has not become smaller than for the ZPG case. This can be explained by the fact that the APG boundary layer has a larger mean flow gradient $\partial U_1/\partial x_2$ in the region $0.1 < x_2/\delta < 0.3$ than the ZPG boundary

American Institute of Aeronautics and Astronautics

layer, where the contribution plays a major role on the spectral peak, and a larger $\partial U_1/\partial x_2$ leads to a larger level of p_{ms}. Note, the level of p_{tt} for isotropic turbulence from the previous work of Hu $et\ al.$[40] is smaller than the present calculation. The reason is that the mirrored source or Green function should be antisymmetric mirrored when dealing with terms including derivative in the wall-normal direction, otherwise the contribution from these terms will be canceled by the source and the mirrored source. This was incorrectly implemented in the previous work.
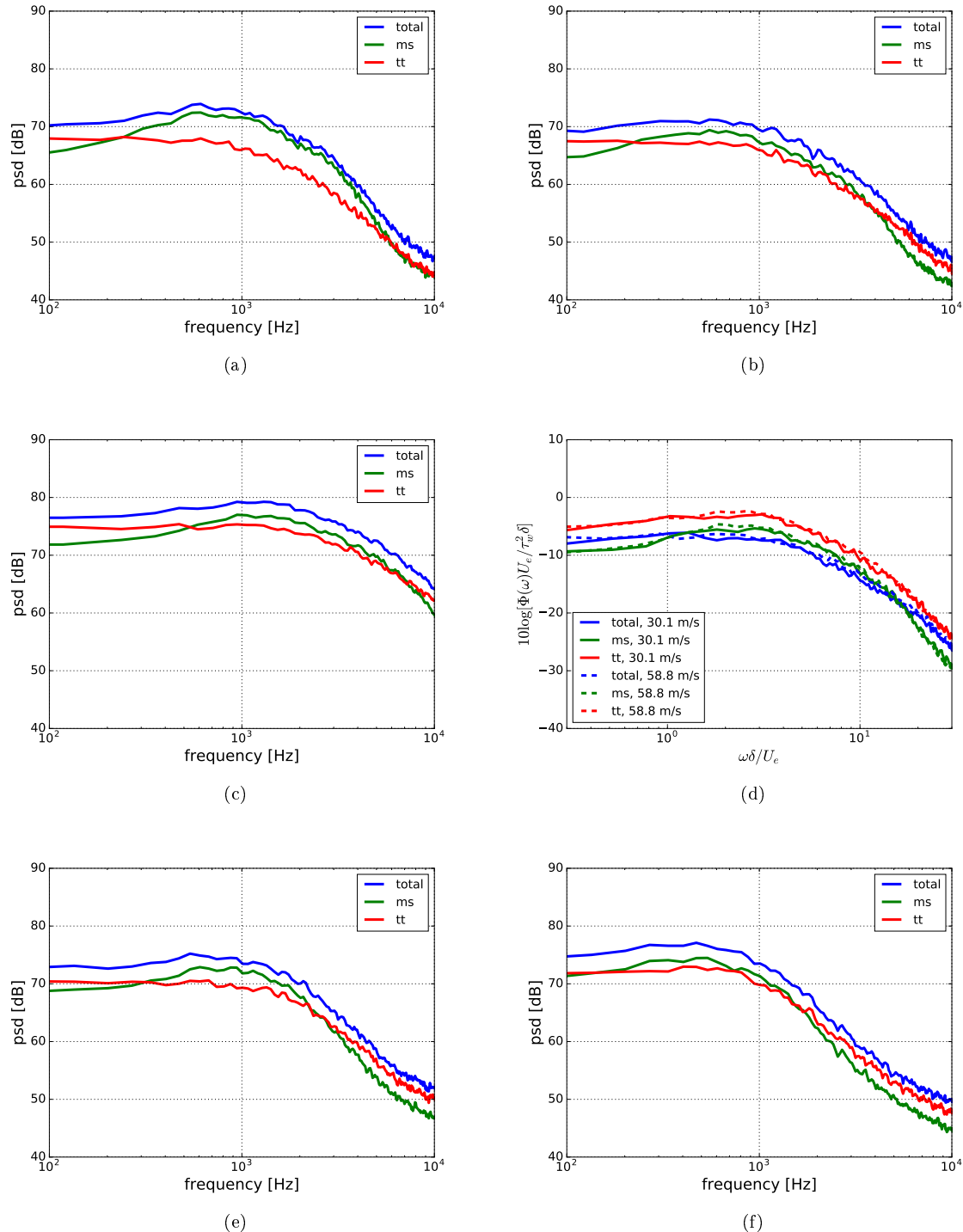
Figure 5: One-point spectra of p_{ms}, p_{tt} and p_{total}; anisotropic turbulence approach for (b-f); (a) ZPG for 30.1 m/s calculated with the isotropic turbulence approach; (b) ZPG for 30.1 m/s; (c) ZPG for 58.8 m/s; (d) scaling for ZPG cases; (e) APG for $x_1 = 1128$ mm; (f) APG for $x_1 = 1210$ mm.

The simulated spectra of p_{total} calculated with the anisotropic turbulence approach are compared to the experimental results, shown in Fig. 6. The spectral trends at low and medium frequencies and the

American Institute of Aeronautics and Astronautics

maximum level of the simulated spectra are well predicted. However, the simulated spectra drop too fast at high frequencies. This is primarily due to the lack of reconstructed kinetic energy in the near wall region $< 0.1\delta$, which contributes mostly to high frequencies. Note that, the RANS calculation over-predicts the kinetic energy level for the APG case, which can lead to an over-prediction of the spectral level. However, the boundary layer thickness for the simulated APG boundary layer is much thinner than in the measured case, which can cause a spectral shift to higher frequencies and a possible spectral level decrease. In any case, the development of the APG spectra which shift to lower frequencies in the downstream direction is well represented.
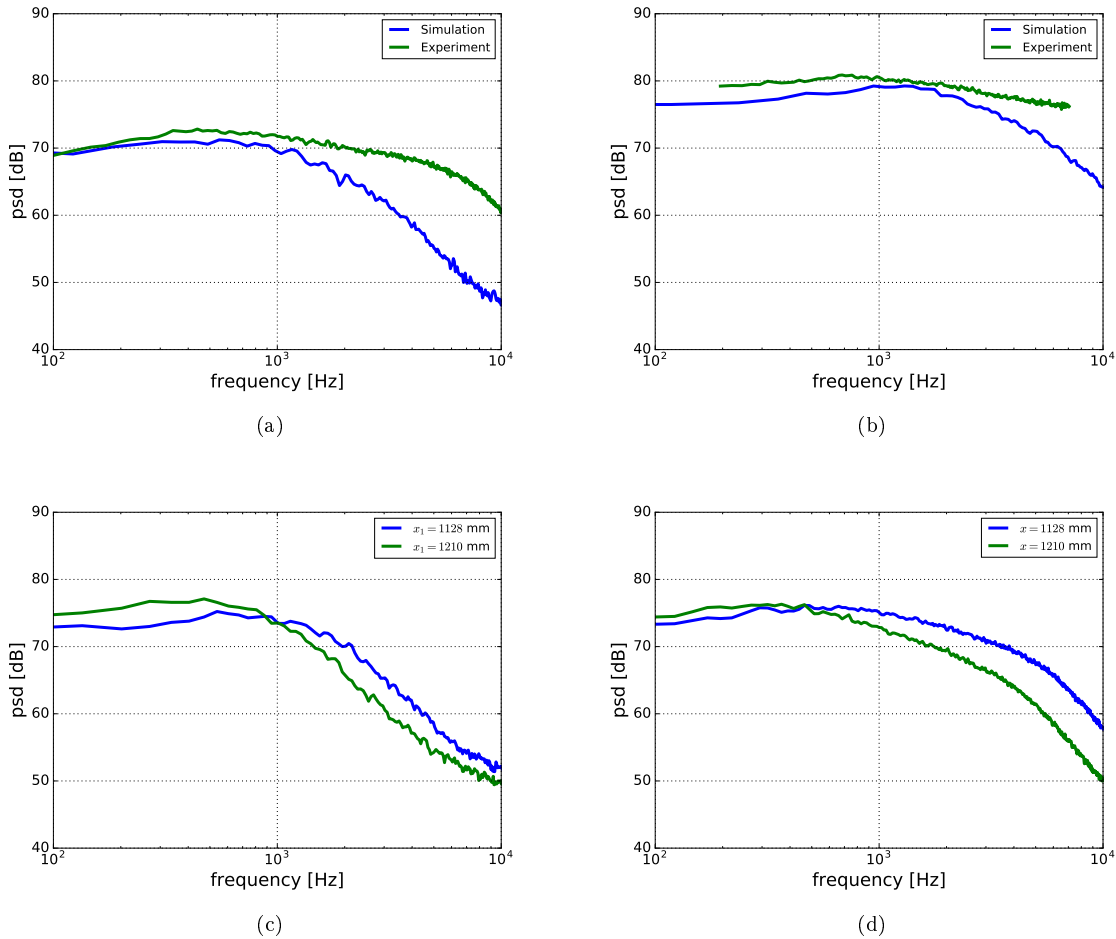

Figure 6: Comparison between one-point spectra calculated with the anisotropic turbulence approach and the measured spectra; (a) ZPG for 30.1 m/s; (b) ZPG for 58.5 m/s; (c) APG, simulated spectra; (d) APG, measured spectra.

C. Cross spectra and convective velocities

The spatial and temporal features of the wall pressure fluctuations can be studied from the two-point statistics. The time-space correlation of the pressure fluctuations is defined by

$$R_{pp}(\mathbf{x}, \mathbf{r}, \tau) = < p(\mathbf{x}, t)p(\mathbf{x} + \mathbf{r}, t + \tau) > . \tag{15}$$

For a slowly growing boundary layer, e.g. the calculated domain of the ZPG boundary layers, the flow field can be treated as a homogeneous field. Thus, $R_{pp}(\mathbf{x}, \mathbf{r}, \tau) \simeq R_{pp}(\mathbf{r}, \tau)$. Cross spectra can be calculated by taking Fourier transform of τ for the time-space correlation $R_{pp}(\mathbf{r}, \tau)$, as follows

$$\Phi_{pp}(\mathbf{r}, \omega) = \frac{1}{2\pi} \int_{-\infty}^{\infty} R_{pp}(\mathbf{r}, \tau) \exp(-i\omega\tau) \, d\tau. \tag{16}$$

American Institute of Aeronautics and Astronautics

If $\mathbf{r} = 0$, we obtain the one-point spectrum $\Phi_{pp}(\omega)$. The coherence spectrum is defined by

$$\Gamma(\mathbf{r},\omega) = \frac{\Phi_{pp}(\mathbf{r},\omega)}{\sqrt{|\Phi_{pp}(\mathbf{0},\omega)|}\sqrt{|\Phi_{pp}(\mathbf{r},\omega)|}}. \tag{17}$$

The coherence spectra from different separations in longitudinal, $\mathbf{r} = r_1 \cdot \mathbf{e}_1$, and the lateral coherence, $\mathbf{r} = r_3 \cdot \mathbf{e}_3$, of the wall pressure fluctuations collapse at medium and high frequencies. At low frequencies the similarity behaviour is lost and the coherence drops. Corcos[23] used exponential functions to characterize the features of the cross spectra by taking advantage of the similarity of the turbulence decay at higher frequencies, reads

$$|\Gamma(r_1, r_3, \omega)| = \exp(-\alpha\omega r_1/U_c)\exp(-\beta\omega r_3/U_c), \tag{18}$$

where U_c is the convective phase velocity, α and β are empirical constants in charge of prescribing the turbulence decay in longitudinal and lateral direction, respectively. A larger value of the constants indicates a more rapid decay of the cross spectra for the wall pressure fluctuations. Hu and Herr[12] measured $\alpha = 0.14$ and 0.125 for the ZPG boundary layers at velocities of 30.2 m/s and 58.7 m/s, respectively. Generally, the value of α depends on the Reynolds number and a larger Reynolds number results in a smaller value. A value of $\beta = 0.72$ was measured for both velocities. For the APG boundary layer the coherence spectra cannot be well characterized with a single exponential curve. However, as convenience for the comparison an exponential function for both longitudinal and lateral direction is drawn from the experiment results. The obtained value of the constants follows $\alpha = 0.23$ and $\beta = 0.55$. Note, the convection of the turbulence flow results in an offset for samples in the streamwise direction and therefore may reduce the longitudinal coherence.[49] To reduce this effect, the time shift between different streamwise positions is calculated using the mean flow velocity $\overline{U}_c(r_1)$ and the time shift is applied to calculate the longitudinal coherence in the present work. In the previous work of Hu and Herr,[12] a larger value of $\alpha = 0.15$ was obtained for the ZPG boundary layer for 30.2 m/s because this effect was not considered.
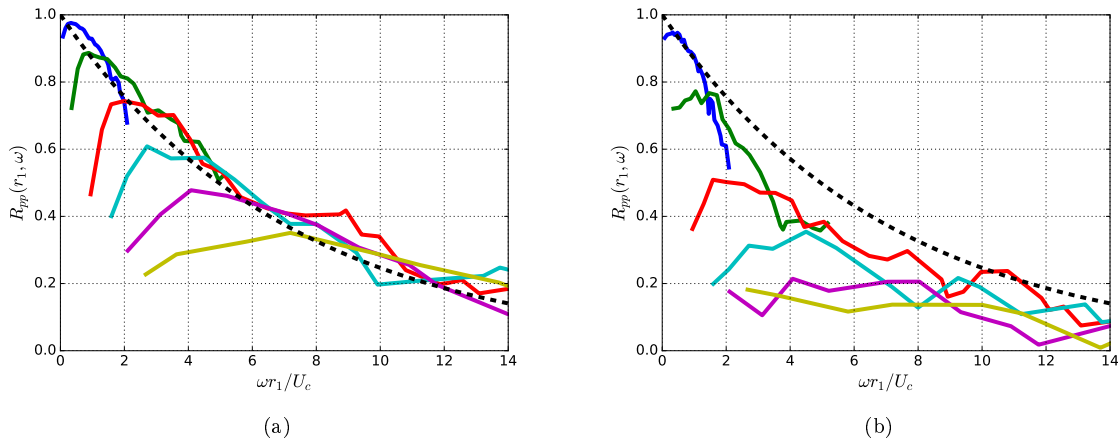

Figure 7: Longitudinal coherence calculated with the anisotropic turbulence apporach, ZPG for 30.1 m/s, $0.6\delta^* < r_1 < 12.6\delta^*$; (-), simulation; (- -), experiment, $\exp(-0.14\omega r_1/U_c)$; (a) p_{ms}; (b) p_{tt}.

Fig. 7 shows the longitudinal coherence of p_{ms} and p_{tt} for the anisotropic turbulence approach as a function of $\omega r_{1,3}/U_c$. A window length of 256 samples for all the cases is used to evaluate the cross spectra. The convective phase velocity U_c is defined by $U_c(r_1,\omega) = r_1\omega/\theta(r_1,\omega)$, where $\theta(r_1,\omega)$ is the phase difference of $\Gamma(r_1, 0, \omega)$. To present the coherence with a separation of r_1 in longitudinal direction, a phase velocity $U_c(r_1,\omega)$ obtained at the same longitudinal separation is used. The results from Fig. 7 show that the decay in streamwise direction from the turbulence-turbulence term p_{tt} is much stronger than for the mean-shear term p_{ms}. The obtained exponential curves from the experiment for prescribing the coherence are also plotted for comparison.

Fig. 8 shows the longitudinal coherence of p_{all}. A very good agreement with the experimental results is obtained for the numerical results with the anisotropic turbulence approach. The results show a much stronger coherence decay for the APG boundary layer than the ZPG boundary layers. Furthermore, a slightly slower decay for the ZPG boundary layer with the higher velocity is also presented in the simulation. The obtained coherence from the isotropic turbulence approach is larger than the one from the anisotropic turbulence approach, see Fig. 8(a,b). This is because for the isotropic turbulence approach p_{ms} is the dominant part (see Fig. 5), which has a larger coherence.
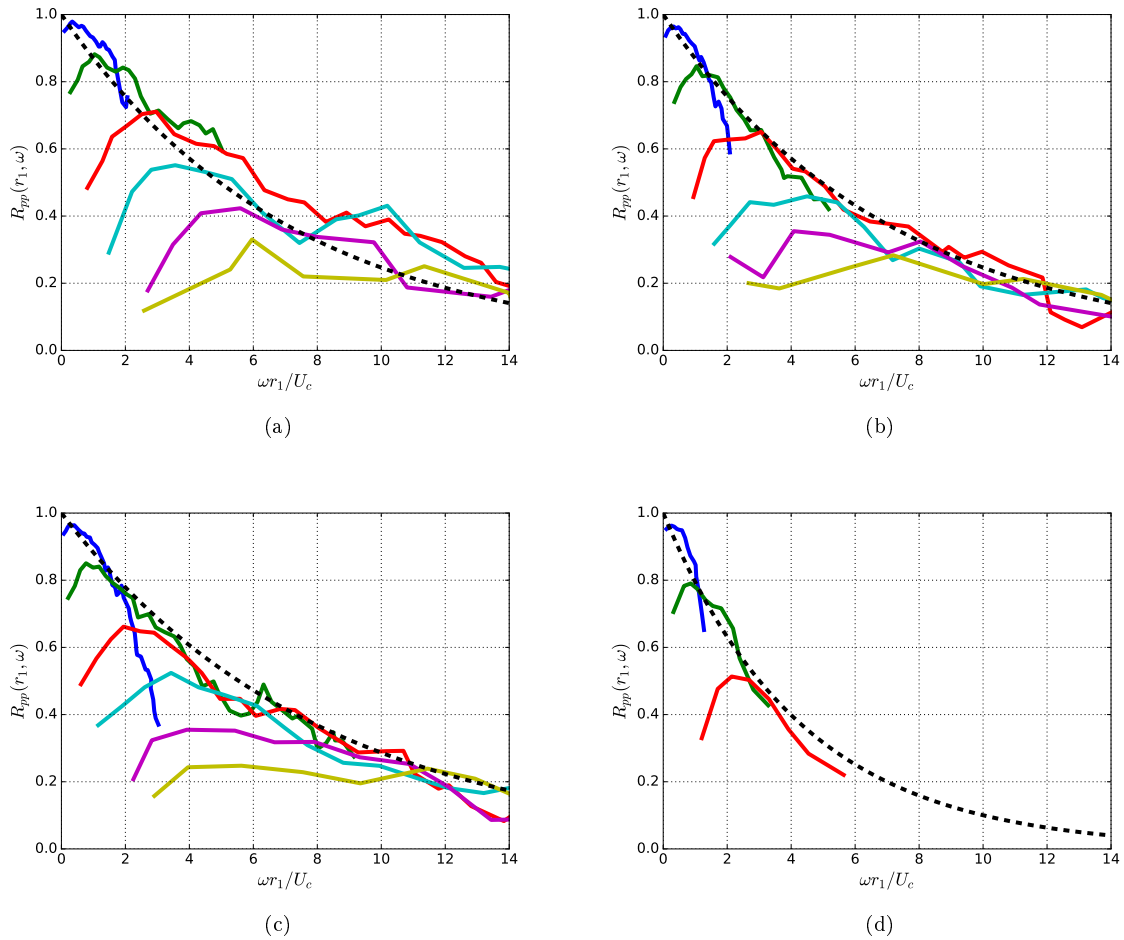
Figure 8: Comparison of the longitudinal coherence, anisotropic turbulence approach for (b-d); (-), simulation for p_{total}; (- -), experiment; (a) ZPG for 30.1 m/s, $0.6\delta^* < r_1 < 12.6\delta^*$, isotropic turbulence approach; (- -), $\exp(-0.14\omega r_1/U_c)$; (b) ZPG for 30.1 m/s, $0.6\delta^* < r_1 < 12.6\delta^*$; (- -), $\exp(-0.14\omega r_1/U_c)$; (c) ZPG for 58.5 m/s, $0.7\delta^* < r_1 < 14.5\delta^*$; (- -), $\exp(-0.125\omega r_1/U_c)$; (d) APG, $0.4\delta^* < r_1 < 3.0\delta^*$; (- -), $\exp(-0.23\omega r_1/U_c)$.
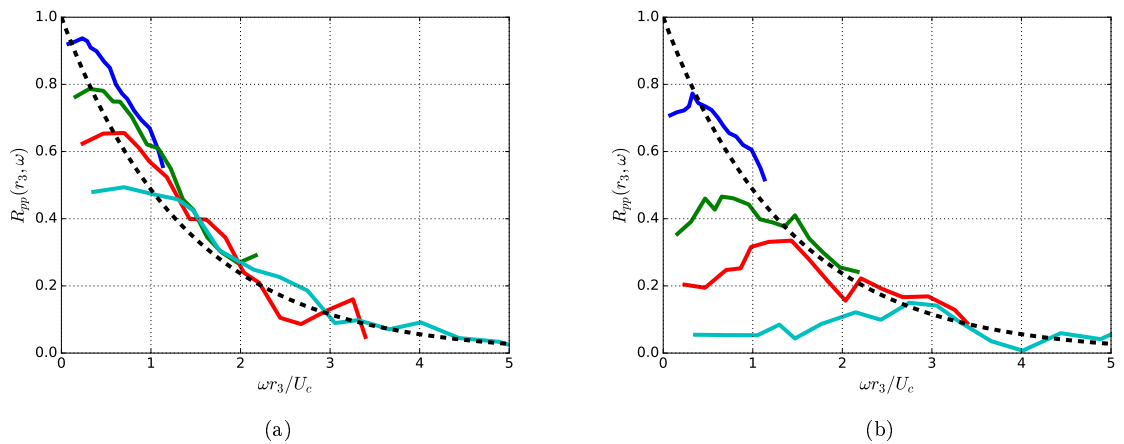

Figure 9: Lateral coherence calculated with the anisotropic turbulence approach, ZPG for 30.1 m/s, $0.6\delta^* < r_3 < 2.7\delta^*$; (-), simulation; (- -), experiment, $\exp(-0.72\omega r_1/U_c)$; (a) p_{ms}; (b) p_{tt}.
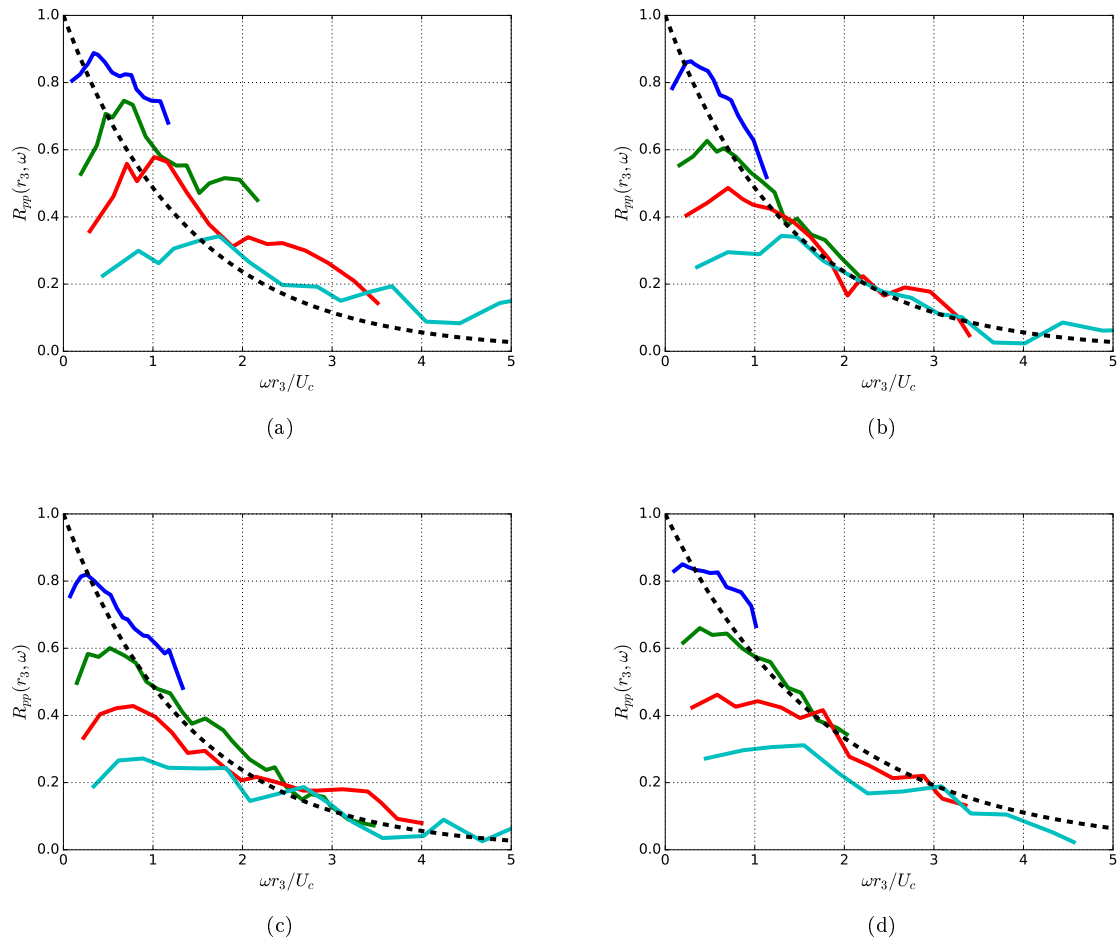
American Institute of Aeronautics and Astronautics

Figure 10: Comparison of the lateral coherence, anisotropic turbulence approach for (b-d); (-), simulation; (- -), experiment; (a) ZPG for 30.1 m/s, $0.6\delta^* < r_3 < 2.7\delta^*$, isotropic turbulence approach; (- -), $\exp(-0.72\omega r_3/U_c)$; (b) ZPG for 30.1 m/s, $0.6\delta^* < r_3 < 2.7\delta^*$; (- -), $\exp(-0.72\omega r_3/U_c)$; (c) ZPG for 58.5 m/s, $0.7\delta^* < r_3 < 3.1\delta^*$; (- -), $\exp(-0.72\omega r_3/U_c)$; (d) APG, $0.4\delta^* < r_3 < 1.8\delta^*$; (- -), $\exp(-0.55\omega r_3/U_c)$.

Fig. 9 shows the lateral coherence of p_{ms} and p_{tt} for the anisotropic turbulence approach as a function of $\omega r_{1,3}/U_c$. The phase velocity U_c does not depend on the lateral separations. A single phase velocity $U_c(\omega)$ obtained by the closest virtual microphones $r_1 = 2$ mm is used to plot the lateral coherence. The same procedure was used to obtain the experimental results for the lateral coherence. The same as the results shown for the longitudinal coherence, the coherence decay of p_{tt} is much stronger than p_{ms} also for the lateral direction.

Fig. 10 shows the obtained lateral coherence compared to the exponential curves which are derived from the measurement. The results for the anisotropic turbulence approach are consistent with the experimental results for all calculated cases. Again, the one with the isotropic turbulence approach shows a larger coherence than the measured curves, which is due to the larger portion of the p_{ms} part. Because p_{ms} has a larger coherence also in the lateral direction shown in Fig. 9.

Fig. 11 shows the comparison of the convective phase velocity for ZPG at velocity of 30.1 m/s. The simulated velocity of p_{total} increases at low frequencies, after reaching the maximum it decreases gradually with increasing frequencies. The maximum velocity is about $0.8U_0$ and located around $\omega\delta/U_0 = 2$. The frequency behaviour and the obtained maximum of the simulated phase velocity show good agreement with the measured results. However, the measured results present an increasing velocity with a larger longitudinal distance. The reason is that the eddies closer to the wall move with a slower velocity and die out over a shorter distance. They contribute to the wall pressure fluctuations not only at high frequencies but also at low frequencies. Thus, a slower velocity over a broadband frequency range was measured at a closer distance. However, this is only poorly presented in the simulation results because of the lack of the realized kinetic energy from FRPM in the near wall region.

A comparison between numerical and experimental obtained phase velocities for ZPG 30.1 m/s and APG 30.4 m/s at $\Delta r_1 = 15$ mm is shown in Fig. 12. The phase velocity for the APG boundary layer is much smaller than the one for the ZPG, which is well presented in the numerical results.

Fig. 13 shows the comparison of the mean convective velocity $\overline{U}_c$, which is obtained by using the time shift τ of the maximum time-space correlation $R_{pp}(r_1, \tau)$ for a fixed longitudinal separation r_1, $\overline{U}_c(r_1) = r_1/\tau(r_1)$. Results for the maximum correlation smaller than 0.03 are not considered. Curves presenting the experimental results are drawn by best fit of the measured data. Simulated mean velocities of p_{total} show similar trends to the measured results. The velocity increases at larger distances and is larger for the ZPG boundary layers than the APG. However, the measured velocities at closer distances are smaller than the simulated results. This is due to the lack of the realized kinetic energy from FRPM in the computation as discussed before. However, the particularly large value obtained for the closest distance also visible for the phase velocity in Fig. 11 is not clear to the authors.
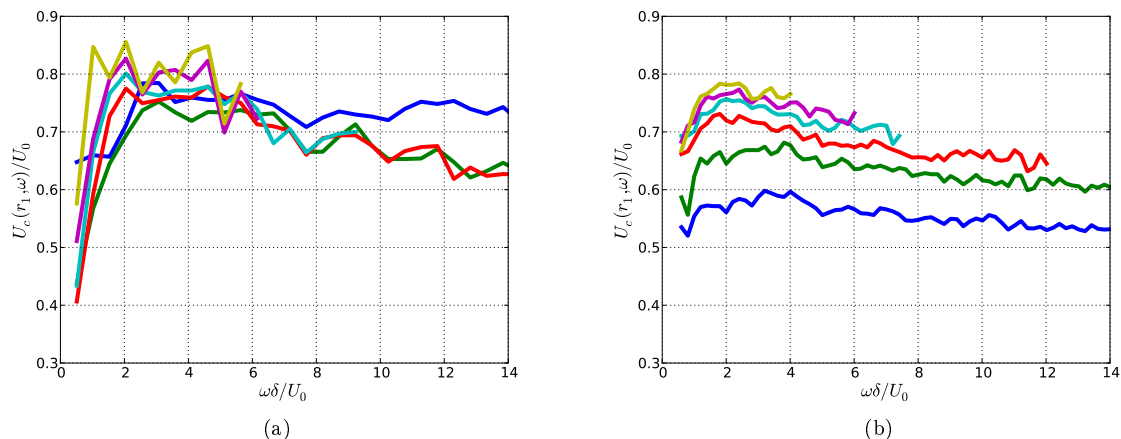

(a)

(b)

Figure 11: Comparison of the convective phase velocity for ZPG at velocity of 30.1 m/s; (a) simulation results calculated with the anisotropic turbulence approach, $0.6\delta^* < r_1 < 18.0\delta^*$; (b) experimental results, $0.6\delta^* < r_1 < 17.1\delta^*$.
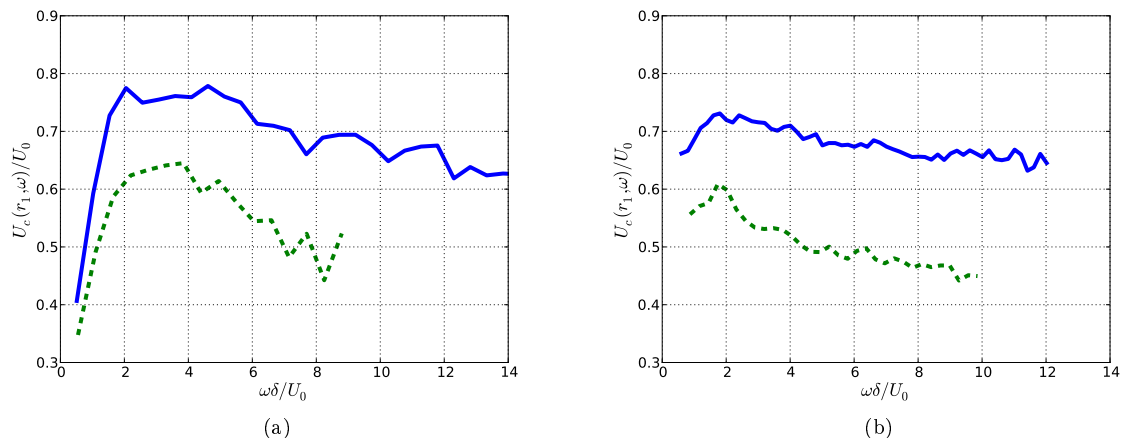

(a)

(b)

Figure 12: Comparison of the convective phase velocity at $\Delta r_1 = 15$ mm; (-), ZPG for 30.1 m/s; (- -), APG for 30.4 m/s; (a) simulation results calculated with the anisotropic turbulence approach; (b) experimental results.

V.   Conclusion

Wall pressure fluctuations beneath zero and adverse pressure gradient turbulent boundary layers are simulated with an effective numerical procedure. A Poisson equation is solved in the wavenumber domain using Hockney's method. The source terms including the mean-shear term and the turbulence-turbulence term on the right-hand side of the equation are realized using synthetic turbulence generated

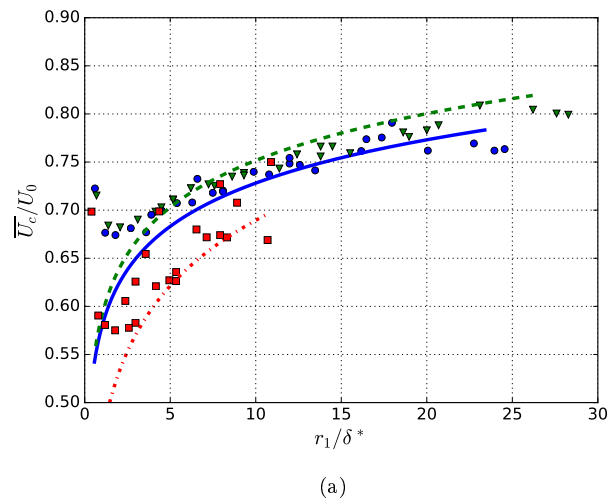American Institute of Aeronautics and Astronautics

(a)

Figure 13: Comparison of the mean convective velocity; anisotropic turbulence approach. ZPG for 30.1 m/s: ●, simulation, (-), experiment; ZPG for 58.8 m/s: ▼, simulation, (- -), experiment; APG: ■, simulation, (-.-), experiment.

by the Fast Random Particle-Mesh Method for both isotropic and anisotropic turbulence approaches. For the anisotropic turbulence approach, anisotropy of the Reynolds stress and the turbulence length scales is applied. The turbulence velocity fluctuations are well realized except for the near wall region, especially for $< 0.1\delta$, where a lack of reconstructed kinetic energy is evident compared to the kinetic energy provided by RANS calculations.

The simulated one-point spectra, cross spectra and convective velocities of the wall pressure fluctuations are compared to the experimental results. The levels and the trends at low and medium frequencies of the one-point spectra are well predicted. An attenuation at higher frequencies is presented which is primarily due to the lack of the realized kinetic energy in the near wall region. This also causes a larger convective velocity at closer longitudinal distances because of the loss of the contributions of eddies closer to the wall, which move slower and die out faster. The major features of the cross spectra and the convective velocities are well determined and consistent with the measured results.

The results show that the mean-shear term and the turbulence-turbulence term have the same order of magnitude for the wall pressure fluctuations if anisotropy of turbulence is considered. For the isotropic turbulence approach, the mean-shear term is the dominant part, which leads to a larger coherence in both longitudinal and lateral directions compared to the anisotropic turbulence approach. This is because the wall pressure fluctuations from the mean-shear term decay slower in longitudinal direction and also has a larger coherence in lateral direction than the turbulence-turbulence term.

References

[1]Blake, W. K., *Mechanics of flow-induced sound and vibration*, Academic Press, Inc., 1986.

[2]Willmarth, W. W. and Wooldridge, C. E., "Measurements of the fluctuating pressure at the wall beneath a thick turbulent boundary layer." *J. Fluid Mech.*, Vol. 14, 1962, pp. 187–210.

[3]Bull, M. K., "Wall pressure fluctuations associated with subsonic turbulent boundary layer flow." *J. Fluid Mech.*, Vol. 28, 1967, pp. 719–754.

[4]Schloemer, H. H., "Effects of pressure gradients on turbulent-boundary-layer wall-pressure fluctuations." *J. Acoust. Soc. Am.*, Vol. 42(1), 1967, pp. 93–113.

[5]Blake, W. K., "Turbulent boundary layer wall pressure fluctuations on smooth or rough walls." *J. Fluid Mech.*, Vol. 44(4), 1970, pp. 637–660.

[6]Farabee, T. M. and Casarella, M. J., "Spectral features of wall pressure fluctuations beneath turbulent boundary layers." *Phys. Fluids*, Vol. A3(10), 1991, pp. 2410–2420.

[7]Leclercq, D. J. J. and Bohineust, X., "Modeling the wave-vector frequency spectrum of turbulent boundary layer wall pressure." *J. Sound Vib.*, Vol. 257(3), 2002, pp. 477–501.

[8]Arguillat, B., Ricot, D., Robert, G., and Bailly, C., "Measurements of wavenumber-frequency spectrum of wall pressure fluctuations under turbulent flows." *AIAA Paper*, 2005.

[9]Ehrenfried, K. and Koop, L., "Experimental study of pressure fluctuations beneath a compressible turbulent boundary layer." *AIAA Paper*, 2008.

[10]Salze, E., Bailly, C., Marsden, O., Jondeau, E., and Juvé, D., "An experimental characterisation of wall pressure wavevector-frequency spectra in the presence of pressure gradients." *AIAA Paper*, 2014.

[11]Catlett, M. R., Forest, J. B., Anderson, J. M., and Stewart, D. O., "Empirical spectral model of surface pressure fluctuations beneath adverse pressure gradients." *AIAA Paper*, 2014.

[12]Hu, N. and Herr, M., "Characteristics of wall pressure fluctuations for a flat plate turbulent boundary layer with pressure gradients." *AIAA Paper*, 2016.

[13]Chase, D. M., "Modeling the wave-vector frequency spectrum of turbulent boundary layer wall pressure." *J. Sound Vib.*, Vol. 70, 1980, pp. 29–68.

[14]Efimtsov, B., "Characteristics of the field of turbulent wall pressure fluctuations at large Reynolds numbers." *Sov. Phys. Acoust*, Vol. 28, 1982, pp. 289–292.

[15]Efimtsov, B., "Similarity criteria for the spectra of wall pressure fluctuations in a turbulent boundary layer." *Sov. Phys. Acoust*, Vol. 30, 1984, pp. 33–35.

[16]Howe, M., *Acoustics of fluid-structure interactions*, Cambridge University Press, 1998.

[17]Smol'yakov, A., "Calculation of the spectra of pseudospund wall-pressure fluctuations in turbulent boundary layers." *Acoustical Physics*, Vol. 3, 2000, pp. 342–347.

[18]Goody, M., "Empirical spectral model of surface pressure fluctuations." *AIAA Journal*, Vol. 42, No.9, 2004.

[19]Rozenberg, Y., Gilles, R., and Moreau, S., "Wall-pressure spectral model including the adverse pressure gradient effects." *AIAA Journal*, Vol. 50(10), 2012, pp. 2168–2179.

[20]Kamruzzaman, M., Bekiropoulos, D., Lutz, T., and Würz, W., "A semi-empirical surface pressure spectrum model for airfoil trailing-edge noise prediciton." *International journal of aeroacoustics*, Vol. 14, 2015.

[21]Catlett, M. R., Anderson, J. M., Forest, J. B., and Stewart, D. O., "Empirical modeling of pressure spectra in adverse pressure gradient turbulent boundary layers." *AIAA Journal*, Vol. 54(2), 2016.

[22]Hu, N., "Empirical spectral model of wall pressure fluctuations including adverse pressure gradient effects." *AIAA Paper*, 2017.

[23]Corcos, G. M., "The structure of the turbulent pressure field in Boundary Layer Flows." *J. Fluid Mech.*, Vol. 18, 1964, pp. 353–378.

[24]Spalart, P. R., "Direct simulation of a turbulent boundary layer up to $Re_\theta = 1410$." *J. Fluid Mech.*, Vol. 187, 1988, pp. 61–98.

[25]Kim, J., "On the structure of pressure fluctuations in simulated turbulent channel flow." *J. Fluid Mech.*, Vol. 205, 1989, pp. 421–451.

[26]Choi, H. and Moin, P., "On the space-time characteristics of wall-pressure fluctuations." *Phys. Fluids*, Vol. A2(8), 1990, pp. 1450–1460.

[27]Na, Y. and Moin, P., "The structure of wall-pressure fluctuations in turbulent boundary layers with adverse pressure gradient and separation." *J. Fluid Mech.*, Vol. 377, 1998, pp. 347–373.

[28]Chang, P. A., Piomelli, U., and Blake, W. K., "Relationship between wall pressure and velocity-field sources." *Phys. Fluids*, Vol. 11, 1999, pp. 3434–3448.

[29]Viazzo, S., Dejoan, A., and Schiestel, R., "Spectral features of the wall-pressure fluctuations in turbulent wall flows with and without perturbations using LES." *J. Heat and Fluid Flow*, Vol. 22, 2001, pp. 39–52.

[30]Jiménez, J., Hoyas, S., Simens, M. P., and Mizuno, Y., "Turbulent boundary layers and channels at moderate Reynolds numbers." *J. Fluid Mech.*, Vol. 657, 2010, pp. 335–360.

[31]Schlatter, P. and Örlü, R., "Assessment of direct numerical simulation data of turbulent boundary layers." *J. Fluid Mech.*, Vol. 659, 2010, pp. 116–126.

[32]Gloefelt, X. and Berland, J., "Turbulent boundary layer wall pressure fluctuations on smooth or rough walls." *J. Fluid Mech.*, Vol. 723, 2013, pp. 318–351.

[33]Eitel-Amor, G., Örlü, R., and Schlatter, P., "Simulation and validation of a spatially evolving turbulent boundary layer up to $Re_\theta = 8300$." *Int. J. Heat Fluid Flow*, Vol. 47, 2014, pp. 57–69.

[34]Sillero, J. A., Jiménez, J., and Moser, R. D., "Two-point statistics for turbulent boundary layers and channels at Reynolds numbers up to $\delta^+ \approx 2000$." *Phys. Fluids*, Vol. 26, 2014, pp. 1–30.

[35]Kraichnan, R. H., "Pressure fluctuations in turbublent flow over a flat plate." *J. Acoust. Soc. Am.*, Vol. 28(3), 1956, pp. 378–390.

[36]Hodgson, T. H., *Pressure fluctuations in shear flow turbulence*, Ph.D. thesis, University of London, 1962.

[37]Meecham, W. C. and Tavis, M. T., "Theoretical pressure correlation functions in turbulent boundary layer." *Phys. Fluids*, Vol. 23, 1980, pp. 1119–1131.

[38]Chang, P. A., "Wavenumber-frequency characteristics of partial wall pressures from large eddy simulations of a turbulent channel flow." Tech. rep., Carderock Division, Naval Surface Warfare Center, 2001.

[39]Hu, N., Reiche, N., and Ewert, R., "Simulation of turbulent boundary layer wall pressure fluctuations via Poisson equation and synthetic turbulence." *(submitted to J. Fluid Mech., 2016)*.

[40]Hu, N., Appel, C., Herr, M., Reiche, N., and Ewert, R., "Numerical study of Wall pressure fluctuations for zero and non-zero pressure gradient turbulent boundary layers." *AIAA Paper*, 2016.

[41]Hockney, R. W. and Eastwood, J. W., *Computer simulation using particles*, Taylor & Francis, Inc., 1988.

[42]Ewert, R., Dierke, J., Siebert, J., Neifeld, A., Appel, C., Siefert, M., and Kornow, O., "CAA broadband noise prediction for aeroacoustic design." *J. Sound Vib.*, Vol. 330, 2011, pp. 4139–4160.

[43]Bailly, C. and Juvé, D., "A stochastic approach to compute subsonic noise using linearized Euler's equations." *AIAA Paper*, 1999.

[44]Tam, C. K. W. and Auriault, L., "Jet mixing noise from fine-scale turbulence." *AIAA Journal*, Vol. 37(2), 1999, pp. 145–153.

[45]Ewert, R., "Broadband slat noise prediction based on CAA and stochasic sound sources from a fast random particle-mesh (RPM) method." *Computers & Fluids*, Vol. 37, 2008, pp. 369–387.

[46]Togiti, V. and Eisfeld, B., "Assessment of g-equation formulation for a second-moment Reynolds stress turbulence model." *AIAA Paper*, 2015.

[47]Mosallem, M. M., "Numerical and experimental investigation of beveled trailing edge flow fields." *Journal of Hydrodynamics*, Vol. 20(3), 2008, pp. 273–279.

[48]Pope, S., *Turbulent flows*, Cambridge University Press, 2000.

[49]Palumbo, D., "Determining correlation and coherence lengths in turbulent boundary layer flight data." *J. Sound Vib.*, Vol. 331, 2012, pp. 3721–3737.